WILEY-VCH

3D and 4D printing of complex structures of Fe–Mn–Si-based shape memory alloy using laser powder bed fusion

Dohyung Kim, Irene Ferretto, Christian Leinenbach*, Wookjin Lee*

D. Kim, Dr. W. Lee
School of Material Science and Engineering, Pusan National University
2, Busandaehak-ro 63beon-gil, Geumjeong-gu, Busan 46241, Republic of Korea
E-mail: wookjin.lee@pusan.ac.kr

I. Ferretto, Dr. C. Leinenbach
Empa-Swiss Federal Laboratories for Material Science and Technology
Überlandstrasse 129, CH-8600 Dübendorf, Switzerland
E-mail: Christian.Leinenbach@empa.ch

Abstract

The additive manufacturing of shape memory materials, commonly known as 4-dimensional (4D) printing, facilitates the achievement of a complex 3-dimensional (3D) structure that possesses a temperature-dependent shape change functionality. Herein, we demonstrate that complex 3D structures of Fe-based shape memory alloys (Fe-SMAs) can be produced through a 3D printing process of laser powder bed fusion (L-PBF). The 3D printed Fe-SMA showed good mechanical properties with much higher strength and stiffness than those in shape memory polymers. The printed Fe-SMAs manifest shape recovery behavior, demonstrating that material-inherent functional behaviors can be combined with the functionalities of the complex 3D structures to facilitate shape morphing, self-healing, and auxetic behavior and to achieve a lattice structure with extraordinary specific strength.

1

1. Introduction

In recent years, numerous efforts have been devoted toward the development of unique three-dimensional (3D) structures with additional functionalities[1–3]. In this type of fusion technique, called 4D printing, a functionality can be induced by adding a fourth axis to 3D spatial axes[4]. In particular, many researchers have attempted the combination of structural functionalities with the inherent functionalities of shape memory materials to achieve shape change or to induce the shape memory effect (SME) [5,6]. For example, Pyo et al. fabricated a shape memory composite in which Ni–Ti shape memory alloy (SMA) wires were embedded in a shape memory polymer (SMP) through fused deposition modeling, which is an 3D printing technique [2]. They demonstrated a reversible actuating component using differences in the transition temperature of SMA and SMP, volume ratio between SMA and SMP, as well as heating and cooling conditions. Cao et al. reported an elastocaloric effect originating from a large transformation entropy change in Ni–Ti SMAs fabricated through laser powder bed fusion (L-PBF)[1]. They showed that aging treatment could lead to the highest elastocaloric performance among those of the SMAs reported in the literature, indicating that the elastocaloric effect achieved in 3D-printed SMAs with a near-net shape allows their outperformance relative to the most efficient elastocaloric cooling devices reported thus far.

In the literature, SMPs have been extensively used for 4D printing owing to their excellent printability and the SME originating from the state transition at the glass transition temperature (T_g) [7–9]. However, the application scope of such SMPs is limited because of their low stiffness and strength. The tensile elastic modulus and tensile yield strength of SMPs are typically lower than 1 GPa and in the range of 1–30 MPa, respectively, which are lower than those of SMAs by one to two orders of magnitude [10]. The application scope of SMPs is further limited by their relatively low T_g of ~95 °C[9]. In contrast, metallic SMAs have a much higher stiffness and strength than SMPs. Typically, the elastic modulus of ferrous SMAs is approximately 200 GPa, and a tensile strength exceeding 1,000 MPa has been reported [11]. In addition, metallic SMAs

have a much larger transformation hysteresis than SMPs, allowing their applicability over a wider temperature range.

Thus far, many types of SMAs with different chemical compositions have been reported in the literature over the past few decades[12–14]. Unlike SMPs, SMAs show not only the SME but also the so-called pseudo-elasticity (PE) functionality, through which an applied deformation is immediately reversed while unloading without any temperature change. Through conventional metallurgical processes other than 3D printing, such as casting, forming, or powder sintering, Ni–Ti-based SMAs [15,16], Cu-based SMAs [17], and Fe-based SMAs (Fe-SMAs) [18] have been extensively developed. Among them, Ni–Ti-based SMAs are the most widely used alloys for 3D printing because they induce the SME and PE as well as exhibit good bio-compatibility. Most previous studies have attempted the 3D printing of SMAs through laser powder bed fusion (L-PBF), rather than methods such as electron beam melting or direct energy deposition, because L-PBF offers high dimensional accuracy without the need for a vacuum environment. In this regard, for instance, Obeidi et al. fabricated rectangular samples of the Ni–Ti SMA on a 316L substrate through L-PBF under various laser conditions to investigate the optimal density and properties [19]. Furthermore, Mahmoudi et al. reported on the printability of the Ni–Ti SMA by using simple brick-shaped samples fabricated through L-PBF under various laser conditions [20].

Although a few papers have reported on the basic properties of Ni–Ti SMAs produced through L-PBF with simple rectangle-like shapes, the fabrication of complex 3D structures of Ni–Ti SMAs with the desired functionalities remains challenging because Ni–Ti-based SMAs have a critical drawback of very high sensitivity to composition change. Although a slight change in chemical composition is unavoidable during the L-PBF process, a compositional change of less than 0.1 wt.% of the Ni–Ti alloy can result in a significant change in the SME and mechanical performance [21,22]. This behavior leads to a very narrow process window for the L-PBF of the Ni–Ti alloy. Consequently, it is almost impossible to optimize the L-PBF conditions under

3

which an Ni–Ti alloy with the desired microstructure and chemical composition and high dimensional accuracy can be produced. Thus, no previous study has successfully fabricated complex 3D structures of Ni–Ti SMAs with good functionalities.

In comparison to Ni–Ti SMAs, the SME and mechanical properties of Fe-Mn-Si based SMAs are less sensitive to compositional change [23]; thus, they can be considered as a candidate for printable SMAs. Fe-SMAs have attracted a considerable attention as a cost-effective alternative to the Ni-Ti alloys over the past two decades [11-13, 23]. Fe-SMAs exhibit high stiffness and yield strength and high recovery stress [24] and induce a strong SME [25]. It has been known that the SME of the Fe-SMAs can be further enhanced when fine precipitations such as NbC or VC are distributed in the microstructures [12,13]. Very recently, we successfully fabricated an Fe-17Mn-5Si-10Cr-4Ni (wt.%) alloy via L-PBF for the first time, which showed a strong SME and high mechanical strength even though the alloy did not contain any carbide forming element for enhancing the SME by the fine precipitations [18].

The main motivation of this work is to apply the L-PBF process to produce complex 3D structures of the Fe-SMA for fabricating novel functional structures. For this purpose, various functional 3D structures of the Fe-SMA were 3D printed to demonstrate the possibility of fabricating complex 3D structures of the Fe-SMA near-freely by the L-PBF, which can open new possibilities in the manufacturing of novel functional structures such as metamaterial structures, artificial muscles, self-healing devices, and 4D-printed structures. To our knowledge, the present study is the first attempt to demonstrate the functional properties of a printed SMA.

2. Results and Discussion

2.1. Mechanical properties and shape memory behavior
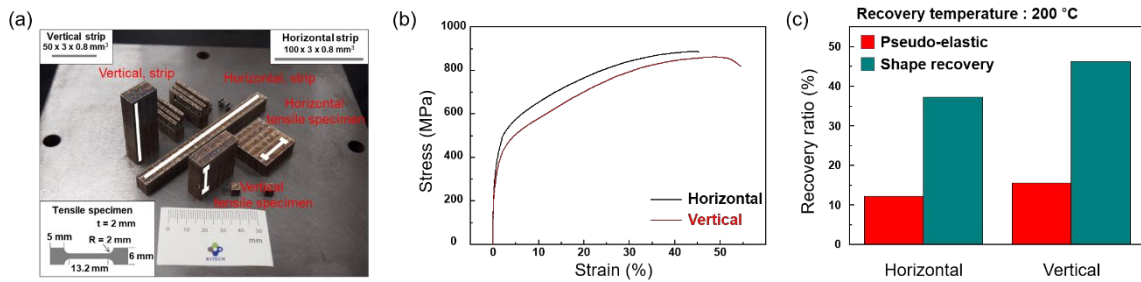
Figure 1. (a) Appearance, (b) tensile stress–strain curves, and (c) shape memory properties of Fe-SMA samples printed through L-PBF.

To investigate the shape recovery and tensile mechanical properties of 3D-printed Fe-SMAs, simple rectangular blocks were fabricated via L-PBF, as shown in **Figure 1**a, using a commercial L-PBF machine (Sodick OPM 250L, Japan) with a laser power of 420 W. Here, we used the pre-alloyed Fe-SMA powder that had been used in our previous work [18]. Moreover, L-PBF conditions (e.g., laser scanning speed) were carefully adjusted to avoid any microstructural defects such as cracks and pores. The microstructures of the as-fabricated Fe-SMAs consisted of both brittle bcc-δ and ductile fcc-γ phases. Because microstructures that almost completely consist of the fcc-γ phase are desired for inducing the shape memory behavior [18], the printed Fe-SMA blocks were heat treated at 800 °C for 30 min to eliminate the bcc-δ phase. The experimental results of changes in microstructure and shape memory responses due to the heat treatment are presented in **Supporting Information.** It indicates that heat treatment at 800°C for 30 min results in a microstructure consisting of fcc-γ and hcp-ε phases without bcc-δ. Due to the absence of the bcc-δ phase, the heat treated samples showed much higher SME than in the as-fabricated state. Subsequently, strips for bending shape recovery tests and dog-bone-shaped tensile specimens were machined from the printed blocks via an electrical discharge machining method. Details of the L-PBF conditions as well as the

microstructures of the Fe-SMAs before and after the heat treatment are provided in the **Supporting Information**. As shown in **Figure 1**a, we fabricated samples in two different directions, namely, horizontal and vertical to the L-PBF building direction. Owing to the limited volume of the raw powder material, the height of blocks used for producing the vertical bending strips was limited to 50 mm, resulting in shorter bending strips in the vertical direction than those in the horizontal direction.

    Figure 1b shows representative tensile stress–stain curves of the L-PBF-printed Fe-SMAs. At the beginning of the loading, the Fe-SMA showed rapid and linear increase of the stress with the strain indicating an elastic deformation. Then, the stress-strain responses became non-linear, which were attributed to the combined plastic deformation and gradual phase transformation from fcc-γ to hcp-ε [18,26]. In this regime, the stress increased gradually with the strain due to the work-hardening effect up to failure. The 0.2% proof yield strengths of the tensile samples machined in horizontal and vertical directions to thse L-PBF building direction were 267 and 230 MPa, respectively. The maximum elongations of the Fe-SMAs in the two directions were 45.3% and 54.4%, respectively. Although the yield strength values are slightly lower than those obtained for conventionally processed Fe-SMAs [23,27], they are at least three times higher than the highest-ever reported value (70 MPa) for SMPs [9]. The slight difference in the tensile behavior due to the vertical and horizontal directions may have originated from the strong crystallographic texture of the Fe-SMA produced through L-PBF [18,28].

    Figure 1c shows the recovery ratios for PE and shape recoveries (i.e., the ratio of the bending strain for PE and shape recovery to the applied bending strain) for the Fe-SMA strips fabricated in the two directions. The samples were bent with a bending strain of 5.26%, unloaded, and heated to 200 °C. The samples fabricated in both directions showed pronounced PE and SME, indicating that the L-PBF-printed Fe-SMA is fully functional after L-PBF and the heat treatment. The shape recovery ratios of the samples in the vertical and horizontal directions were approximately 36% and 47%, respectively. In contrast, the reported values for the bending

shape recovery ratio of the conventionally processed Fe-17Mn-5Si-10Cr-4Ni-(V,C) are 25%–35% [29]. Even though the addition of V and C in the Fe-SMA is known to have a positive effect on the SME due to the presence of VC precipitations [29], the 3D printed Fe-SMA in this study showed higher SME than the conventionally processed VC containing alloy regardless of the sample orientation. This behavior is ascribed to a high density of stacking faults and extremely thin hcp-ε phases in the 3D printed Fe-SMA as reported in our previous study [28]. The stacking faults and extremely thin hcp-ε phases have been known for easy nucleation sites for stress-induced hcp-ε phase resulting in high SME [30]. Thus, the results presented in **Figure 1**c indicate that the shape recovery performance of the L-PBF-printed Fe-SMA is comparable or even higher than that of the conventionally processed Fe-SMA.
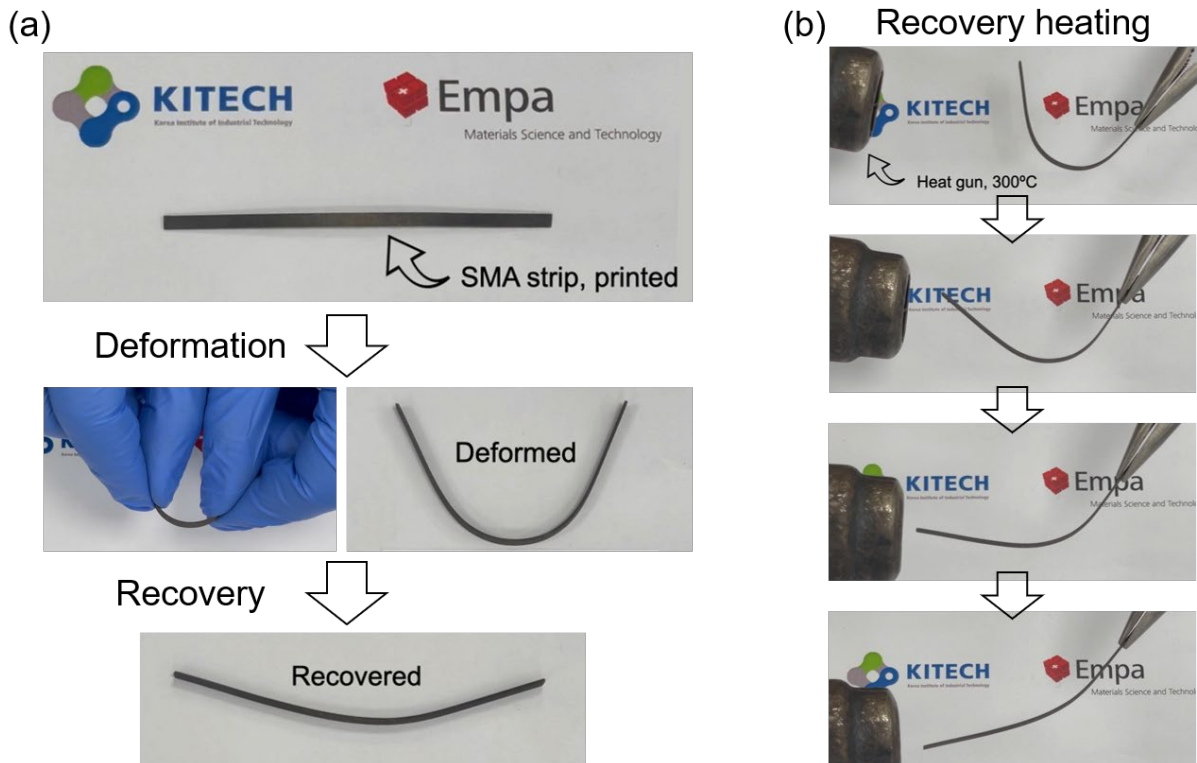

Figure 2. Progress of shape recovery of an Fe-SMA strip produced in the horizontal direction. (a) Experimental procedure and (b) stages of shape recovery.

Figure 2 shows the progress of the shape recovery process of an Fe-SMA strip produced in the horizontal direction; the strip was heated to 300 °C using a heat gun after bending deformation. The complete procedure is shown in **Movie S1**, **Supporting Information.** The bending deformation of the strip could be easily achieved without any serious damage, as shown in **Figure 2**a. The shape recovery process during heating is shown in **Figure 2**b. The shape of the bent strip recovered almost immediately upon heating. As shown in **Movie S1**, **Supporting Information,** the entire recovery process shown in **Figure 2**b took less than 5 s, suggesting that the shape recovery process of the L-PBF-printed Fe-SMA occurs rapidly.
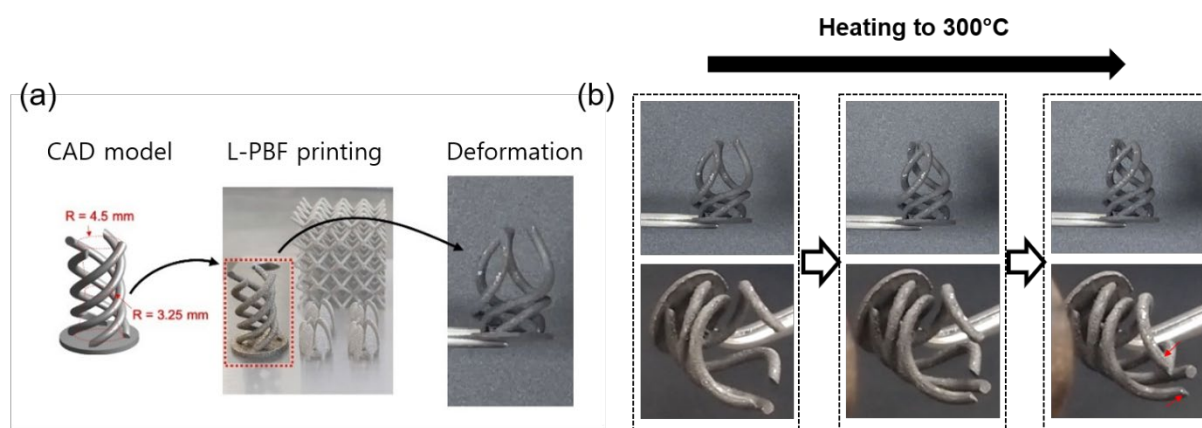
2.2. Shape morphing behavior

Shape morphing is defined as the continuous shape change of a single-material component. Shape morphing techniques have been applied for the development of aircraft systems to improve their aerodynamic performance and reduce cost, drag, and noise by eliminating open gaps [31]. Conventionally, Ni–Ti SMAs have been extensively used for morphing actuators [32]. In addition, SMAs have been regarded as candidates for smart solar shading materials [33] with the shape morphing functionality. In this regard, the 4D printing of the SMA can produce complex self-actuating or biomimetic structures. In this section, we examine the possibilities of using a printed Fe-SMA for shape morphing.
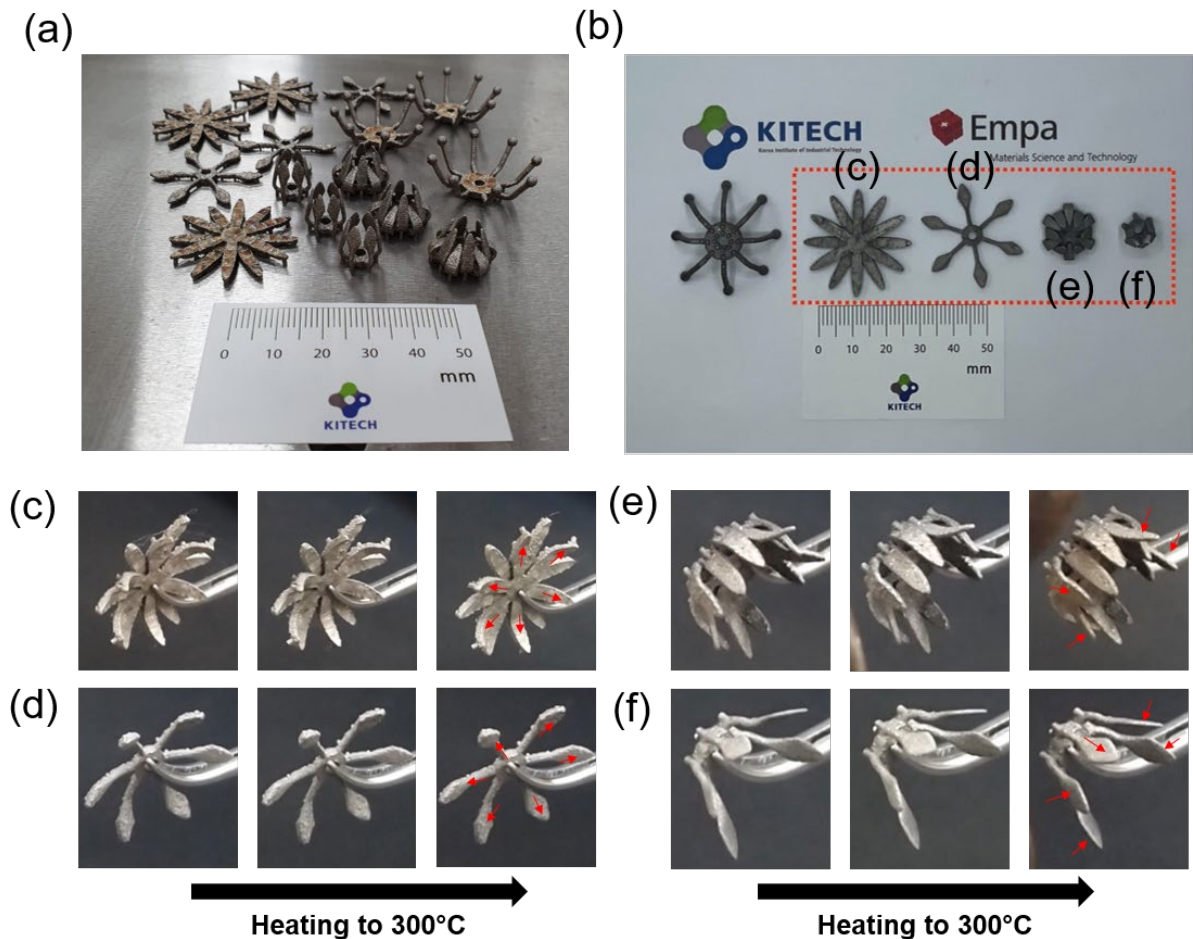
Figure 3. Shape morphing behavior of flower-like Fe-SMA samples produced by L-PBF. (a, b) Appearances of samples in the as-built state. (c–f) Shape morphing upon the heating of samples with (c, d) open leaves and (e, f) closed leaves.

For demonstration purposes, various flower-like samples were prepared, as shown in **Figure 3**a and b. Samples with four different geometries were printed through L-PBF. Among them, two samples had opened leaves and the other two had closed leaves under the as-fabricated condition, as indicated by **Figure 3**(c, d) and (e, f), respectively. After detachment from the baseplate, the samples were heat treated at 800 °C for 30 min (all experiments reported in the succeeding sections were conducted after the heat treatment). Subsequently, for samples with leaves originally in the closed position, the leaves were mechanically deformed to be in a slightly opened position, and vice versa.

The shape morphing of the four flower-like samples is shown in **Figure 3**c–f. The total recovery amounts differ depending on the sample thickness and shape; higher bending strains are applied on thicker samples. However, all samples clearly showed the shape recovery behavior upon heating (**Movie S2**, **Supporting Information**). All samples immediately began to recover their original shapes when heated. The shape recovery was also completed within a few seconds, implying that the L-PBF-printed Fe-SMAs can exhibit fast shape morphing or actuating performance when adequately deformed and heated.

Figure 4. Shape morphing of a spring-like Fe-SMA sample. (a) Preparation of the sample with computer-aided design (CAD) and L-PBF printing and (b) shape morphing behavior upon heating.

To further demonstrate that shape morphing can be achieved with complex 3D shapes, we printed another artifact, which has a spring-like shape with various internal radii (**Figure 4**a).

The diameter of each spring-like feature in the artifact was 2 mm. Such a complex 3D structure can be easily manufactured through L-PBF, as shown in **Figure 4**a; however, it is very difficult or even impossible to manufacture such complex structures by using methods other than 3D printing, such as casting and machining or hot forming. For demonstration purposes, we randomly deformed the spring-like sample, as shown in **Figure 4**a. Upon heating, the sample immediately began to recover its original shape, as shown in **Figure 4**b and **Movie S3**, **Supporting Information**.

The rapid and clear shape morphing behavior shown in **Figures** 3 and 4 makes L-PBF very attractive for fabrication of Fe-SMAs toward the applications that require strong and fast actuation. Examples of such applications include morphing nozzles [34] and morphing wings [35] in the aerospace field and spoilers in the automotive field [36]. The capability of L-PBF to easily produce complex 3D structures induces advantageous properties in systems used for such applications.

2.3. Metamaterial structures

Negative Poisson's ratio

A metamaterial is a material with unique properties that do not occur in nature. An auxetic structure with a negative Poisson's ratio (NPR) is one of the representative metamaterial structures; it exhibits an increased shear modulus, an increased indentation resistance [37,38], and a high energy absorption capability [39]. Such unique behaviors arise from the specially designed internal structures of metamaterials. The L-PBF of Fe-SMA can easily produce metamaterials with complex internal structures. To show the capability of the 3D-printed Fe-SMAs to achieve complex metamaterial structures, two types of 2D metamaterial structures, namely, re-entrant and S-type metamaterials [40], were produced through L-PBF. The geometries of the metamaterial structures fabricated via the L-PBF of the Fe-SMA are shown in **Figure 5**a. A CAD model and detailed dimensions are shown in **Figure S7**a and b, **Supporting Information**.

A cyclic tensile test was conducted to investigate PE during loading and unloading. In the tests, the cyclic loading and unloading conditions were controlled by tensile crosshead displacement to apply cyclic loads while increasing the applied strain by 1% of the total length of the metamaterial structures. For each cycle, unloading was performed by reducing the applied load to 10 N. Subsequently, the actual applied strain was recalculated on the basis of the local displacements of the upper- and lower-most parts of the metamaterial structures. The local displacements during the cyclic loading tests were measured by using the digital image correlation (DIC) technique.
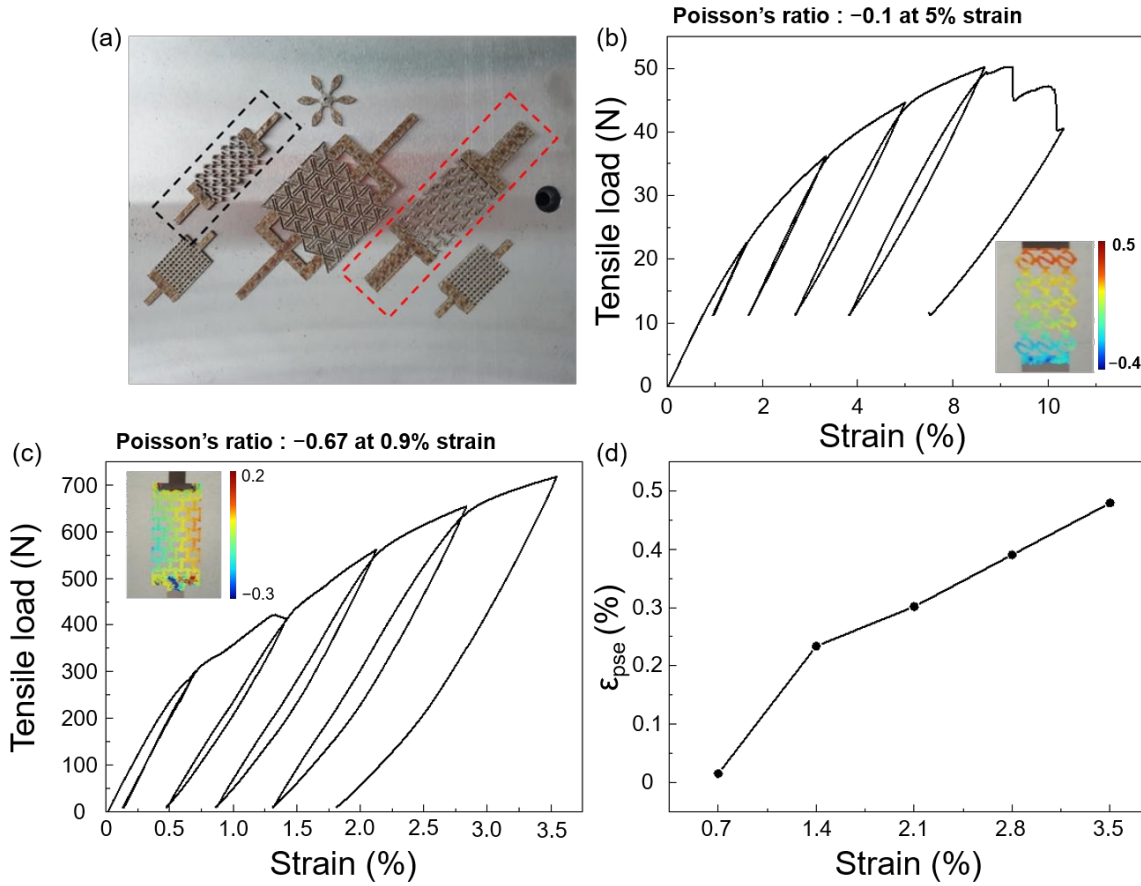
Figure 5. (a) L-PBF-printed Fe-SMA 2D metamaterial structures. The red and black dotted rectangles indicate the re-entrant and S-type samples, respectively. (b, c) Cyclic load–strain curves for the S-type and re-entrant samples. The insets show displacements along lateral directions from DIC calculations. (d) Evolution of PE strains with loading and unloading cycles for the re-entrant sample.

Figure 5b shows a cyclic stress–strain curve from the S-type structure, which is indicated by the black dotted rectangle in **Figure 5**a. For each cyclic load, the actual applied strain was higher than the strain controlled by the displacement of the tensile crosshead because of the deformation of parts other than the metamaterial structure. The loading and unloading curves at high applied strain show clear hysteresis loops, indicating the pronounced PE behavior. Such an interesting behavior is originated because some amount of hcp-ε phase produced while loading transforms back to fcc-γ upon unloading [18]. A sudden drop in the applied load at a strain of approximately 7% is considered an indicator of local fracture. The local strain distribution measured using the DIC at ~5% strain is shown in the inset of **Figure 5**b. It reveals

that the S-type metamaterial structure can effectively translate an applied tensile load to shear deformation. Owing to its internal structure, simple uniaxial tensile loading can produce significant shear motion of the sample, as indicated by negative lateral displacement (i.e., right to left on the figure) in the lower part and positive displacement (i.e., left to right in the figure) in the upper part of the sample. This implies that the upper and lower parts of the sample moved laterally in opposite directions, resulting in the torsional motion of the overall structure. Moreover, the overall Poisson's ratio of the S-type structure was identified as approximately −0.1 through the DIC of the local displacement map at 5% strain. The Poisson's ratio of −0.1 is much smaller than the typical value of approximately 0.33. Detailed results of the DIC analyses to obtain the Poisson's ratios can be found in **Figure S5**, **Supporting Information**.

Figure 5c shows the cyclic tensile test result for the 2D re-entrant structure (sample indicated by the red dotted rectangle in **Figure 5**a). This structure is known to exhibit pronounced NPR behavior [41]. The 2D re-entrant structure also shows pronounced hysteresis loops from the second loading cycle and beyond. Moreover, the DIC result clearly indicates that this structure exhibits NPR behavior. As shown in the inset of the figure, the lateral displacement in the left part of the sample is to the left, and the displacement in the right part of the sample is to the right. This indicates lateral expansion during tensile deformation. The Poisson's ratio measured using DIC at 2.1% strain was approximately −0.67. This implies that, when deformed by tension, the 2D re-entrant structure in this study expands laterally by 67% of its tensile deformation, instead of shrinking. Detailed results of the DIC analyses and the obtained Poisson's ratios can be found in **Figure S6**, **Supporting Information**.

The 2D re-entrant structure showed pronounced PE behavior, as indicated by the hysteresis loops in **Figure 5**c. The evolution of the PE strain (ε_{pse}) of the re-entrant structure is plotted as a function of applied strain in **Figure 5**d. The PE strain is shown to increase almost linearly with the strain applied in the corresponding loading cycle. As the PE is one of the main characteristic behaviors of Fe-SMA, which is associated with reversible phase transformations

upon loading and unloading, this result clearly indicates that the 2D re-entrant metamaterial structure consists of a fully functional Fe-SMA.

The L-PBF of the Fe-SMA enables the production of metamaterial structures with complex shapes, as demonstrated in Figure 5. Furthermore, we showed that metamaterial structures produced using the Fe-SMA can exhibit additional material-inherited functionalities such as PE. Although only two 2D metamaterial structures with simple geometries are shown for demonstration purposes in this study, almost any type of functional metamaterial structures can be produced through the L-PBF of the Fe-SMA. Thus, the proposed method provides a new opportunity for designing and fabricating metamaterial structures. For instance, auxetic structures prepared using the L-PBF-printed Fe-SMA can have a much higher energy absorption capability than simple conventional structures [42]. Because of the presence of such SMA, the performance of auxetic structures is significantly improved owing to the SMA-inherited damping capacity originating from PE behavior [43,44]. Such structures have great potential in applications wherein high damping or energy dissipation behavior is needed.

Shape recovery and self-healing capability
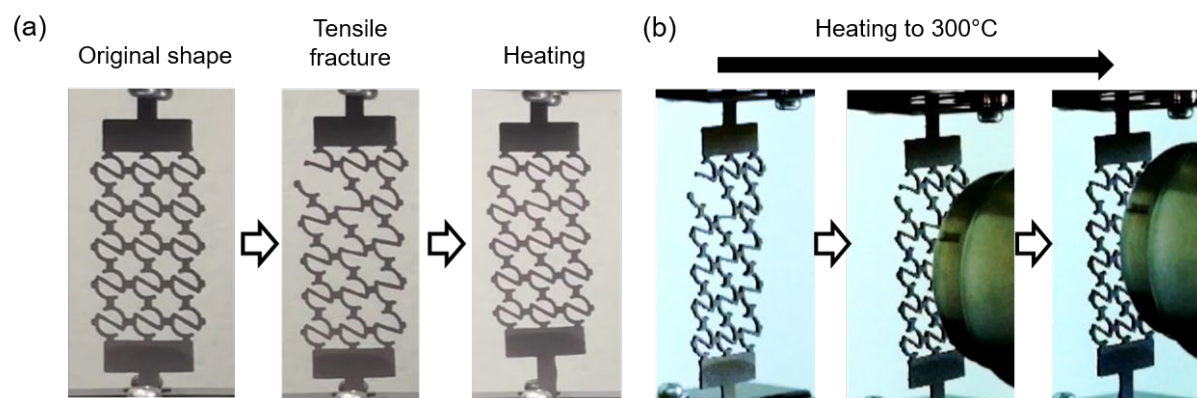
As shown in **Figure 5**, the Poisson's ratio and apparent stiffness of a functional structure consisting of the L-PBF-printed Fe-SMA can be near freely tuned through an appropriate structural design. Moreover, the deformed functional structures can be easily recovered upon heating because of the shape recovery behavior. In addition, the shape recovery behavior of a metamaterial structure can also be tailored by designing its internal structure. To demonstrate the tunability of the shape recovery behavior, the S-type sample after tensile fracture was heated using a heat gun up to 300 °C. Before heating, the sample was strained to 10% tensile elongation, as shown in **Figure 5**b. **Figure 6**a shows the appearances of the sample before and after tensile fracture as well as after heating. In the tensile-fractured state, the local fracture of the sample can be clearly observed in the upper-left side of the figure. Near this area, the sample was considerably deformed because of the uneven load distribution due to local fracture. Upon heating, the original sample structure was almost completely restored. The progress of the shape recovery process upon heating is shown in **Figure 6**b and **Movie S4**, **Supporting Information**. These results clearly indicate that the shape recovery performance of the L-PBF-printed Fe-SMA-based metamaterial can be significantly improved through appropriate structural design

because the maximum recovery strain of the bulk Fe-SMA is considerably lower than 10% (usually approximately 1%) [23].

The excellent shape recovery capability of the Fe-SMA metamaterial provides an interesting opportunity for the development of new self-healing structures. If a structure consists of an Fe-SMA metamaterial with an appropriate design for efficient shape recovery, the original shape of the structure can be easily restored, even after serious structural damage, by simply heating it. The tunability of stiffness, Poisson's ratio, and shape recovery behavior of the metamaterial structures consisting of Fe-SMA also facilitate the development of self-healing polymer composite structures. When a self-healing composite is composed of a self-healing polymer and pre-strained SMA strips, the self-healing efficiency can be significantly improved because the SMA can produce sufficiently large forces for closing cracks [45]. If the Fe-SMA metamaterial structures are used instead of pre-strained SMA strips, the stiffness of the metamaterial structure can be easily adjusted through structure design to achieve more efficient reinforcement, e.g., allowing the structure to be deformed simultaneously with the polymer matrix when the composite deforms. Moreover, the recovery performance of the metamaterial can be tuned to efficiently close the cracks of the polymer matrix.

2.4. Strong artificial muscle effect

3D printing is conducted for the development of actuators for soft robotics, such as artificial muscles that can perform self-sensing or actuation upon external stimuli. Kim et al. demonstrated actuation for various motions by using a partly activating circumferentially and longitudinally arranged Ni–Ti SMA wire around a soft mesh tube [46]. Kong et al. reported that woven Ni–Ti SMA wires could lift up weights when the wires were activated by electrical heating [47]. For application to artificial muscles, the recovery stress (i.e., the stress that can be generated by shape recovery) must be sufficiently high to achieve the desired functionality, e.g., to grab an object with sufficient force or to lift a dead weight. The printed Fe-SMA is a very good candidate for making strong artificial muscles because it is as stiff as steel and has a tensile yield strength of >400 MPa. The conventionally processed Fe-SMAs with a chemical composition similar to that used in this study have been successfully applied for generating compressive stress on a concrete civil structure because it can produce a high recovery stress of >500 MPa [48]. To demonstrate the applicability of the printed Fe-SMA structures as artificial muscles, we prepared a spider-like sample via L-PBF.

Under the as-fabricated condition, the spider-like feature has eight radially outstretched, folded legs with an angle of 120° (a CAD model and detailed dimensions are shown in **Figure S8**, **Supporting Information**). The structure is specially designed to support a large load stably by its legs and to translate effectively the shape recovery induced bending motions of the legs to a lifting motion of the overall structure. The lateral size of the sample was 38.3 mm. The cross-sectional area of each leg was 1.5×2.0 mm^2, and the total weight of the sample was ~5 g. After heat treatment, the legs were straightened. Subsequently, the sample was placed on a steel plate and connected to a steel wire with a load of 2 kg, as shown in **Figure 7**. It can be clearly observed that the small spider-like sample with a self-weight of ~5 g can support a 2 kg load, approximately 400 times the weight of the sample, without any serious damage to the sample structure.
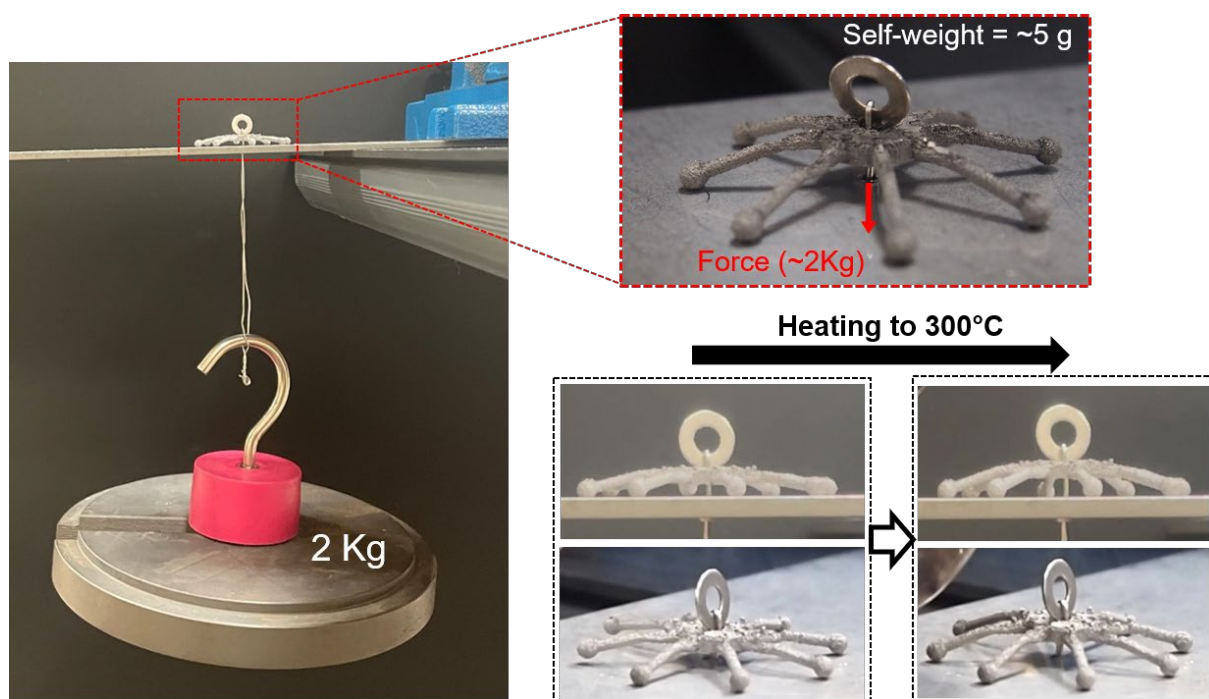
Figure 7. Artificial muscle effect due to the shape recovery of a spider-like L-PBF-printed Fe-SMA sample.

Upon heating to 300 °C, the original shape was restored, causing the 2 kg weight to be lifted up against gravitational force (**Figure 7** and **Movie S5**, **Supporting Information**). This implies that the small spider-like sample can generate a sufficiently large recovery stress to lift the load. The fact that a 5 g sample of the Fe-SMA can lift a 400 times heavier weight indicates that the printed Fe-SMAs can be used as strong artificial muscles, actuator components, or high-precision clamping components. Another advantage of using the printed Fe-SMA in artificial muscle devices is that nearly any shape or structure can be easily fabricated using the near-net-shaping process of L-PBF. For instance, a conventionally manufactured artificial muscle device made of the Ni–Ti SMA wires required complex coiling and weaving process for production [45]. However, such complex processes are not needed when conducting L-PBF for the 3D printing of the Fe-SMA. Artificial muscles of nearly any shape can be easily achieved through L-PBF, and the device will be fully functional after a simple heat treatment.

2.5. Lattice structure
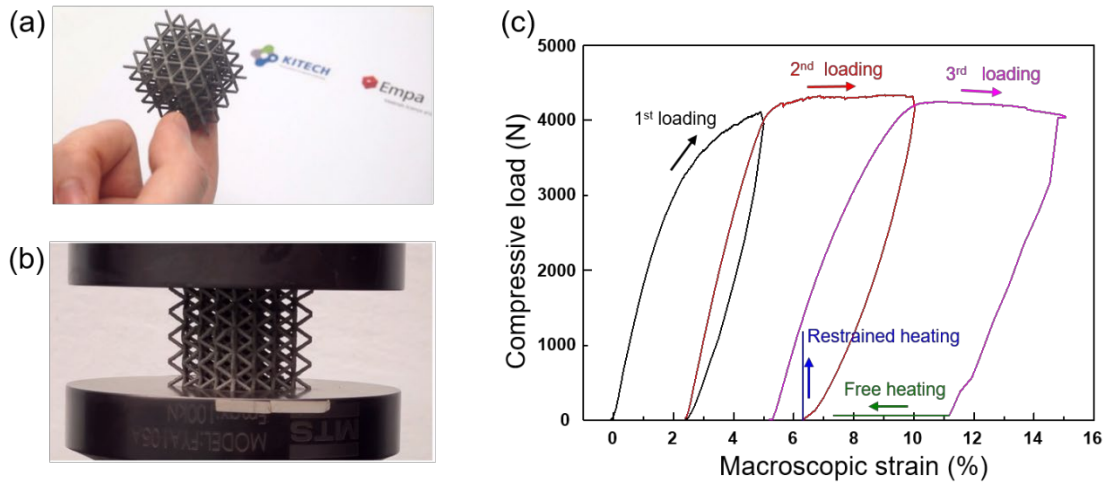
Figure 8. Cyclic compression and shape recovery test of an Fe-SMA lattice structure. (a) Fe-SMA lattice structure produced through L-PBF. (b) Experimental set up for the compressive test. (c) Load–strain curve obtained from the cyclic compression and shape recovery test.

One of the most extensively studied functional structures fabricated using 3D printing is the so-called lattice structure. Lattice structures are composed of struts or thin faces that are connected with specific unit-cell geometries. The major advantage of the lattice structure for structural use is that it can exhibit both lightweight and high strength as well as the capability of energy impact absorption [49]. Lattice structures have been used in biomedical applications for producing metallic components with stiffness close to that of the human bone [50] and in the aerospace industry for developing systems with a high specific strength [51]. When lattice structures are produced by using the SMA, additional material-inherited functionalities such as PE and SME are expected to be induced, thereby producing a structure with a combination of functionalities such as shape memory and high specific strength.

To investigate the possibility of enhancing the functionalities of Fe-SMA for use in the fabrication of the lattice structure, a lattice-structure-type sample was produced through L-PBF, as shown in **Figure 8**a. The weight of the sample was 21 g, which is light enough to be supported easily by one finger. The sample had a strut-based body-centered cubic structure with a strut diameter of 1 mm and a lattice unit-cell length of 7.5 mm. In total, the sample had 4 × 4

× 4 unit cells. Thus, the overall dimensions of the lattice structure sample were $30 \times 30 \times 30$ mm^3. Furthermore, the porosity and total weight of the lattice structure sample were 90.88% and 21 g, respectively (a CAD model and detailed dimensions can be found in **Figure S9**, **Supporting Information**). The detailed dimensional accuracy and surface quality of the lattice structure were shown in **Figure S10, Supporting Information**.

The mechanical properties and shape memory behavior of the Fe-SMA-based lattice structure were evaluated through a specially designed cyclic compression test. The experimental set up is shown in **Figure 8**b. At the first loading cycle, a macroscopic strain (i.e., compressive deformation of the lattice structure over its total length in the direction of compression) of 5% was applied. As shown in **Figure 8**c, the lattice structure deformed elastically with a linear increase in the load with macroscopic strain, up to an applied load of ~2,200 N. Subsequently, the structure deformed non-linearly, indicating plastic deformation. Assuming that the lattice structure is a bulk material with a cross-sectional area of 30×30 mm^2, the macroscopic yield strength is estimated to be ~2.44 MPa. This strength is higher than that (1–1.5 MPa) of similar lattice structures with a porosity of 87.4% that were made of stainless steel with a bulk yield strength of 725 MPa [52]. The macroscopic compression modulus observed in the first loading cycle was ~190 MPa, which is approximately 1000 times lower than the elastic modulus of the Fe-SMA in the bulk form. This indicates that the physical properties of the Fe-SMA, such as apparent density, apparent elastic modulus, and yield strength, can be tailored by the appropriate design of the lattice structure and by fabrication through L-PBF.

The load applied in the first loading cycle was removed by unloading, followed by the application of a load of up to 10% in the second cycle. Loading and unloading curves at this stage clearly showed the hysteretic behavior, as shown in **Figure 8**c, indicating that each strut in the Fe-SMA lattice structure individually acts as an SMA beam. In the second loading cycle, a plateau appeared at approximately 4000 N, implying that the overall lattice structure plastically deformed under this loading condition. The unloading curve after the second loading

showed a pronounced non-linear behavior arising from PE behavior. After unloading, the sample was heated to 300 °C by using a heat gun under a restrained condition (i.e., under a fixed overall length) to investigate the behavior of recovery force generation. The heating of the lattice structure with deformation in the compressive direction restrained by a compression plate generated a recovery force over 1,100 N, as shown in **Figure 8**c. This result indicates that the SME was successfully induced upon heating. Moreover, this small lattice structure with a self-weight of 21 g can lift loads greater than 110 kg.

After unloading the generated force, a compressive load of up to 15% was applied in the third cycle. There was a decreasing trend in the applied load during the third loading cycle, revealing that some Fe-SMA struts in the lattice structure started to fracture at this stage of loading. However, the overall structure did not collapse up to a macroscopic strain of 15%. The unloading curve in the third cycle also showed a massive recovery from 15% to ~11%, which may have been caused by both the PE and structural flexibility of the lattice structure. After unloading, the sample was again heated to 300 °C by using the heat gun. In the free-standing state, the deformation of the lattice structure was further recovered by approximately 4% upon heating. Such a large recovery strain may also have arisen from the combination of the material-inherited SMA and the structural flexibility of the lattice structure.

The results of the cyclic compressive test of the Fe-SMA lattice structure clearly demonstrate that the L-PBF 3D printing of the Fe-SMA lattice structure allows us to access additional functionalities of the material. Design freedom of the lattice structure enables us to control the physical and functional properties of the Fe-SMA structures; therefore, they can be used to develop a new functional structure. For instance, highly flexible Fe-SMA lattice structures with an appropriate elastic modulus can be used as new damping materials. Moreover, it is worth highlighting that open-pore structures with controlled physical and functional properties can be easily designed and used for the development of new functional composite structures. Polymeric composites embedding a pre-deformed Fe-SMA lattice structure can generate an

internally controlled residual stress state by activating the SME of the Fe-SMA structure via

simple heating.

3. Conclusions and Outlook

In this study, <mark>for the first time</mark> we successfully produced complex 3D shapes of the Fe-SMA with the full shape memory functionality by conducting L-PBF. We demonstrated that the L-PBF-printed Fe-SMA having excellent mechanical properties can be very easily functionalized with a simple heat treatment after L-PBF. <mark>The excellent properties of the Fe-SMA produced by the L-PBF together with the new design capability of the smart structures will open up new possibilities for the researches and applications.</mark> The main conclusions are summarized as follows:

1. Through L-PBF, a fully functional Fe-SMA having excellent mechanical properties was successfully fabricated. By a simple heat treatment at 800 °C for 30 min after L-PBF, a yield strength of >230 MPa with a maximum elongation of >50% was achieved. <mark>Such a strength is at least three times higher than the highest-ever reported value (70 MPa) for SMPs.</mark> When a bending pre-strain of 5.26% was applied at room temperature, the original shape of the L-PBF-processed 3D-printed Fe-SMA was immediately recovered after applied bending deformation of more than 10% while unloading because of its PE. Pronounced shape recoveries of 36% and 47% of the applied bending strain, in directions perpendicular and parallel to the L-PBF building direction, respectively, were observed upon heating the deformed Fe-SMA to 200 °C.

2. <mark>We demonstrated that complex 3D structures of the Fe-MSA can be made by the L-PBF in nearly any shape. Moreover,</mark> we successfully demonstrated the pronounced shape recovery behavior of Fe-SMAs with complex 3D shapes produced through L-PBF. The original structures of differently shaped flower-like Fe-SMA samples could be recovered upon heating, indicating that the L-PBF of Fe-SMAs can be used as the so-called 4D printing technology. Moreover, the shape morphing capability of the Fe-SMA was successfully demonstrated by using a spring-like sample.

3. Functional metamaterial structures with shape memory functionalities can be easily produced via the L-PBF of Fe-SMA. For demonstration, two types of 2D metamaterial structures of Fe-SMA were fabricated and tested. The metamaterial structures showed functionalities originating from their unique shapes, e.g., an NPR, as well as functionalities originating from the SME.

4. The shape memory behavior of the Fe-SMA can be substantially strengthened through appropriate structural design, resulting the production of the material in precise shapes via L-PBF. For instance, the original shape of an S-type 2D metamaterial structure could be almost recovered although some parts of the structure were broken during deformation with a very large strain of 20%. Such behavior can be used to efficiently close cracks in self-healing composites.

5. The excellent combination of the high strength and shape memory behavior of the Fe-SMA produced through L-PBF induced a high recovery stress. A specially designed spider-like sample with a weight of only 5 g could lift a load greater than 2 kg due to the shape recovery stress. Such a high recovery stress will be very useful for the L-PBF of the Fe-SMA used in artificial muscles or actuating components.

6. The mechanical properties of the Fe-SMA can be tailored by introducing specially designed internal patterns in the lattice structures. In this study, a strut-based body-centered cubic lattice structure of Fe-SMA, with a porosity of 90.88%, was successfully fabricated through L-PBF. Owing to its internal structure, the Fe-SMA lattice structure macroscopically behaved completely differently from the bulk Fe-SMA. It showed a yield strength of 2.44 MPa and a compressive elastic modulus of 190 MPa, as well as large hysteretic behavior upon cyclic loading and shape recovery behavior. The additional functionalities that can be obtained from the design of the lattice structure can expand the use of Fe-SMA in the fabrication of functional structures such as structural dampers.

4. Experimental Section/Methods

Sample preparation: Pre-alloyed Fe-17Mn-5Si-10Cr-4Ni (wt.%) powder (Metal Player Co., Ltd, Republic of Korea) produced by gas atomization in an Ar atmosphere was used as the starting material for L-PBF, as in our previous work [13]. All 3D-printed samples were fabricated using an OPM250L L-PBF machine (Sodick Co., Ltd, Japan) equipped with an ytterbium fiber laser with a wavelength of 1,070 nm and a maximum laser output of 500 W (YLR-500-WC, IPG, Laser GmbH, Germany). The laser spot has a Gaussian beam distribution and a size of 200 μm. Printing was performed at a scanning speed (v) of 800 mm/s, hatch spacing (h) of 0.1 mm, layer thickness (t) of 0.05 mm, and laser power of 420 W. The corresponding volumetric energy density (VED), defined as $VED = P/v \cdot h \cdot t$, was 105 J/mm^3. During the L-PBF of each layer, additional laser contour scanning was conducted with the same laser power along the contour line after the core part of each layer was laser-scanned to enhance the dimensional quality of the final L-PBF samples. A bidirectional laser scan strategy with a 90° rotation between the layers was applied for all samples. All printed Fe-SMA samples were heat treated at 800 °C for 30 min to eliminate the primary bcc-δ phase and to improve shape recovery. Detailed procedures for optimizing the L-PBF conditions as well as microstructural changes in terms of the L-PBF conditions are presented in the **Supporting Information**.

Tensile and compression tests: Uniaxial tensile tests were performed to characterize the strength of dog-bone-shaped samples by using an RB 301 UNITECH-T universal testing machine (R&B Inc., Republic of Korea) at a speed of 1 mm/min. Cyclic tensile tests for samples with 2D structures were performed using AGS-X (SIMAZU Inc., Japan) with a crosshead speed of 3×10^{-4} mm/min. A cyclic compression test of the lattice structure sample was conducted using E45 (MTS Corp., USA) at a speed of 3×10^{-4} mm/min. Complex 2D and 3D samples produced via L-PBF were heated using a GHG 630 heat gun (Robert Bosch GmbH, Germany).

Bending recovery tests: Three-point bending tests with a pre-defined deformation radius were performed using the strip samples shown in **Figure 1**a. The samples for bending recovery tests were bent using a mold to a radius of 7.6 mm along the neutral axis at room temperature, as schematically shown in **Figure 9**. The pre-strain, ε_{pre} (applied bending strain), i.e., the maximum tensile and compressive strains at the top and bottom surfaces of the strips, was calculated as follows:

$$\varepsilon_{pre} = \frac{t}{2 \cdot R_b}, \quad (1)$$

where R_b is the bending radius of the strip at its neutral axis and t is the strip thickness. In our case, the bending radius and strip thickness were 7.2 and 0.8 mm, respectively. Therefore, ε_{pre} calculated using **Equation 1** was approximately 5.26%.

The bending PE strain, ε_{pse}, was calculated by using the bend radius, R_u, after unloading as follows:

$$\varepsilon_{pse} = \varepsilon_{pre} - \frac{t}{2 \cdot R_u}, \quad (2)$$

Subsequently, shape recovery tests were performed by heating the bent strips to 200 °C in an electric furnace under atmospheric conditions for 10 min. The shape recovery strain, ε_{recs}, was determined as follows:

$$\varepsilon_{rec} = \varepsilon_{pre} - \varepsilon_{pse} - \frac{t}{2 \cdot R_h}, \quad (3)$$

where R_h is the bend radius of the strip after heating to 200 °C and cooling to room temperature. The recovery ratios shown in **Figure 1**c were calculated using the $\varepsilon_{rec}/\varepsilon_{pre}$ and $\varepsilon_{pse}/\varepsilon_{pre}$ ratios for the shape recovery and PE, respectively.
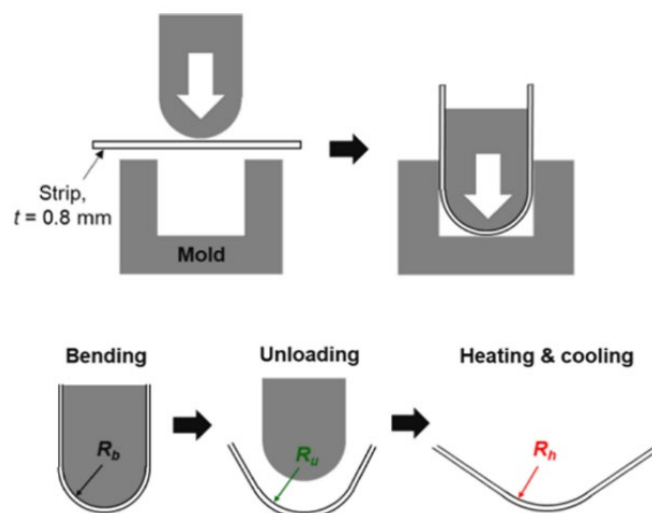
Figure 9. Schematic diagram of the bending recovery test [27].

WILEY-VCH

Supporting Information

Supporting Information is available from the Wiley Online Library or from the author.

References

[1]   Y. Cao, X. Zhou, D. Cong, H. Zheng, Y. Cao, Z. Nie, Z. Chen, S. Li, N. Xu, Z. Gao, W. Cai, Y. Wang, *Acta Mater.* **2020**, *194*, 178.

[2]   Y. Pyo, M. Kang, J. young Jang, Y. Park, Y. H. Son, M. C. Choi, J. wan Ha, Y. W. Chang, C. S. Lee, *Sensors Actuators, A Phys.* **2018**, *283*, 187.

[3]   T. Gustmann, F. Gutmann, F. Wenz, P. Koch, R. Stelzer, W. G. Drossel, H. Korn, *Prog. Addit. Manuf.* **2020**, *5*, 11.

[4]   X. Kuang, D. J. Roach, J. Wu, C. M. Hamel, Z. Ding, T. Wang, M. L. Dunn, H. J. Qi, *Adv. Funct. Mater.* **2019**, *29*, 1.

[5]   J. Fu, Z. Hu, X. Song, W. Zhai, Y. Long, H. Li, M. Fu, *Opt. Laser Technol.* **2020**, *131*, 106374.

[6]   M. Elahinia, N. Shayesteh Moghaddam, A. Amerinatanzi, S. Saedi, G. P. Toker, H. Karaca, G. S. Bigelow, O. Benafan, *Scr. Mater.* **2018**, *145*, 90.

[7]   Y. Y. C. Choong, S. Maleksaeedi, H. Eng, J. Wei, P. C. Su, *Mater. Des.* **2017**, *126*, 219.

[8]   H. Y. Jeong, S. C. An, I. C. Seo, E. Lee, S. Ha, N. Kim, Y. C. Jun, *Sci. Rep.* **2019**, *9*, 1.

[9]   A. Li, A. Challapalli, G. Li, *Sci. Rep.* **2019**, *9*, 1.

[10]   J. Sun, Y. Liu, J. Leng, *http://dx.doi.org/10.1177/1045389X14546658* **2014**, *26*, 2020.

[11]   W. J. Lee, B. Weber, C. Leinenbach, *Constr. Build. Mater.* **2015**, *95*, 600.

[12]   Z. Dong, U. E. Klotz, C. Leinenbach, A. Bergamini, C. Czaderski, M. Motavalli, *Adv. Eng. Mater.* **2009**, *11*, 40.

[13]   S. Kajiwara, D. Liu, T. Kikuchi, N. Shinya, *Scr. Mater.* **2001**, *44*, 2809.

[14]   Y. H. Wen, H. B. Peng, P. P. Sun, G. Liu, N. Li, *Scr. Mater.* **2010**, *62*, 55.

[15]   Q. Zhang, S. Hao, Y. Liu, Z. Xiong, W. Guo, Y. Yang, Y. Ren, L. Cui, L. Ren, Z. Zhang, *Appl. Mater. Today* **2020**, *19*, 100547.

[16] C. A. Biffi, J. Fiocchi, F. Valenza, P. Bassani, A. Tuissi, *Shape Mem. Superelasticity* **2020**, *6*, 342.

[17] T. Gustmann, H. Schwab, U. Kühn, S. Pauly, *Mater. Des.* **2018**, *153*, 129.

[18] I. Ferretto, D. Kim, N. M. Della Ventura, M. Shahverdi, W. Lee, C. Leinenbach, *Addit. Manuf.* **2021**, *46*, 102071.

[19] M. A. Obeidi, M. Monu, C. Hughes, D. Bourke, M. N. Dogu, J. Francis, M. Zhang, I. U. Ahad, D. Brabazon, *J. Mater. Res. Technol.* **2021**, *14*, 2554.

[20] M. Mahmoudi, G. Tapia, B. Franco, J. Ma, R. Arroyave, I. Karaman, A. Elwany, *J. Manuf. Process.* **2018**, *35*, 672.

[21] Y. Yang, J. B. Zhan, J. B. Sui, C. Q. Li, K. Yang, P. Castany, T. Gloriant, *Scr. Mater.* **2020**, *188*, 130.

[22] J. Sam, B. Franco, J. Ma, I. Karaman, A. Elwany, J. H. Mabe, *Scr. Mater.* **2018**, *146*, 164.

[23] W. J. Lee, B. Weber, G. Feltrin, C. Czaderski, M. Motavalli, C. Leinenbach, *Mater. Sci. Eng. A* **2013**, *581*, 1.

[24] Y. Yang, A. Arabi-Hashemi, C. Leinenbach, M. Shahverdi, *Mater. Sci. Eng. A* **2021**, *802*, 140694.

[25] H. Peng, G. Wang, S. Wang, J. Chen, I. MacLaren, Y. Wen, *Mater. Sci. Eng. A* **2018**, *712*, 37.

[26] L. Chengxin, W. Guixin, W. Yandong, L. Qingsuo, Z. Jianjun, *Mater. Sci. Eng. A* **2006**, *438–440*, 808.

[27] D. Kim, C. Park, J. Lee, K. Hong, Y. Park, W. Lee, *Eng. Struct.* **2021**, *239*, 112300.

[28] D. Kim, I. Ferretto, J. B. Jeon, C. Leinenbach, W. Lee, *J. Mater. Res. Technol.* **2021**, *14*, 2782.

[29] C. Leinenbach, H. Kramer, C. Bernhard, D. Eifler, *Adv. Eng. Mater.* **2012**, *14*, 62.

[30] S. Kajiwara, *Mater. Sci. Eng. A* **1999**, *273–275*, 67.

[31] C. Thill, J. Etches, I. Bond, K. Potter, P. Weaver, *Aeronaut. J.* **2008**, *112*, 117.

[32] J. Sun, Q. Guan, Y. Liu, J. Leng, *J. Intell. Mater. Syst. Struct.* **2016**, *27*, 2289.

[33] F. Fiorito, M. Sauchelli, D. Arroyo, M. Pesenti, M. Imperadori, G. Masera, G. Ranzi, *Renew. Sustain. Energy Rev.* **2016**, *55*, 863.

[34] J. Mabe, *Proc. - Eur. Conf. Noise Control* **2008**, 5487.

[35] A. A. Karakalas, T. T. Machairas, D. A. Saravanos, *J. Intell. Mater. Syst. Struct.* **2019**, *30*, 1682.

[36] A. Sellitto, A. Riccio, *Materials (Basel).* **2019**, *12*, DOI 10.3390/ma12050708.

[37] K. E. Evans, A. Alderson, *Adv. Mater.* **2000**, *12*, 617.

[38] K. E. Evans, K. L. Alderson, *Eng. Sci. Educ. J.* **2000**, *9*, 148.

[39] F. Scarpa, L. G. Ciffo, J. R. Yates, *Smart Mater. Struct.* **2004**, *13*, 49.

[40] K. Meena, S. Singamneni, *Mater. Des.* **2019**, *173*, 107779.

[41] T. Fey, F. Eichhorn, G. Han, K. Ebert, M. Wegener, A. Roosen, K. I. Kakimoto, P. Greil, *Smart Mater. Struct.* **2015**, *25*, 15017.

[42] H. Hassanin, A. Abena, M. A. Elsayed, K. Essa, *Micromachines* **2020**, *11*, 1.

[43] T. Sawaguchi, T. Maruyama, H. Otsuka, A. Kushibe, Y. Inoue, K. Tsuzaki, *Mater. Trans.* **2016**, *57*, 283.

[44] F. Yoshinaka, T. Sawaguchi, N. Ilya, S. Takamori, N. Nagashima, *Procedia Struct. Integr.* **2019**, *19*, 214.

[45] G. R. Aghamirzadeh, S. M. R. Khalili, R. Eslami-Farsani, A. Saeedi, *Polym. Compos.* **2019**, *40*, 1883.

[46] S. Kim, E. Hawkes, K. Cho, M. Jolda, J. Foley, R. Wood, *2009 IEEE/RSJ Int. Conf. Intell. Robot. Syst. IROS 2009* **2009**, 2228.

[47] X. Kong, H. Jin, Y. Chen, J. Yang, E. Dong, *2018 IEEE Int. Conf. Robot. Biomimetics, ROBIO 2018* **2018**, 1202.

[48] A. Arabi-Hashemi, W. J. J. Lee, C. Leinenbach, *Mater. Des.* **2018**, *139*, 258.

[49] C. Bellini, R. Borrelli, V. Di Cocco, S. Franchitti, F. Iacoviello, L. Sorrentino, *Fatigue Fract. Eng. Mater. Struct.* **2021**, 1.

[50] C. de Formanoir, G. Martin, F. Prima, S. Y. P. Allain, T. Dessolier, F. Sun, S. Vivès, B. Hary, Y. Bréchet, S. Godet, *Acta Mater.* **2019**, *162*, 149.

[51] O. Rehme, C. Emmelmann, *Laser-based Micropackaging* **2006**, *6107*, 61070K.

[52] T. Zhong, K. He, H. Li, L. Yang, *Mater. Des.* **2019**, *181*, 108076.